Available online at www.sciencedirect.com
ScienceDirect
Trans. Nonferrous Met. Soc. China 30(2020) 2188−2199
Transactions of Nonferrous Metals Society of China
www.tnmsc.cn

# Preparation and electrochemical performance of nitrogen-doped carbon-coated $Bi_2Mn_4O_{10}$ anode materials for lithium-ion batteries

Jing ZHAN[1,2], Chang-fan XU[1], Yi-yu LONG[1], Qi-hou LI[1]

1. School of Metallurgy and Environment, Central South University, Changsha 410083, China
2. National Engineering Laboratory for High Efficiency Recovery of Refractory Nonferrous Metals Resources, Central South University, Changsha 410083, China

Received 1 January 2020; accepted 4 June 2020

**Abstract:** To inhibit rapid capacity attenuation of $Bi_2Mn_4O_{10}$ anode material in high-energy lithium-ion batteries, a novel high-purity anode composite material $Bi_2Mn_4O_{10}$/ECP-N (ECP-N: N-doped Ketjen black) was prepared via an uncomplicated ball milling method. The as-synthesized $Bi_2Mn_4O_{10}$/ECP-N composite demonstrated a great reversible specific capacity of 576.2 mA·h/g after 100 cycles at 0.2*C* with a large capacity retention of 75%. However, the capacity retention of individual $Bi_2Mn_4O_{10}$ was only 27%. Even at 3*C*, a superior rate capacity of 236.1 mA·h/g was retained. Those remarkable electrochemical performances could give the credit to the introduction of ECP-N, which not only effectively improves the specific surface area to buffer volume expansion and enhances conductivity and wettability of composites but also accelerates the ion transfer and the reversible conversion reaction.
**Key words:** $Bi_2Mn_4O_{10}$ nanoparticles; N-doped Ketjen black; rate capability; lithium-ion batteries

## 1 Introduction

Higher requirements have been put forward for the lithium-ion batteries (LIBs) with higher energy and power density, as well as more excellent cycle performance because of the rapid development of portable electronic equipment and electric vehicles and the limited theoretical specific capacity of commercial graphite anodes (372 mA·h/g) [1,2]. Among a multitude of anode materials, manganese-based oxides, such as MnO [3], $Mn_2O_3$ [4], $MnO_2$ [5] have attracted tremendous research attention owing to their stable chemical states, environmental friendliness, low cost, and high specific capacities between 600 and 1000 mA·h/g [6]. Particularly, the metallic Bi can furnish a desirable volumetric capacity of 3760 mA·h/cm$^3$. Bi-based materials, as anode materials for LIBs, have also exhibited distinctive characteristics of excellent volumetric density and specific capacity due to their tailor-made morphologies, microstructures, and multifarious composition [7−9]. For example, $Bi_2O_3$/rGO composite anode materials showed a specific capacity of 347.3 mA·h/g after 100 electrochemical cycles at 1*C* [10]. However, most metal oxides generally display low conductivity, and their commercial application is severely impeded by dreadful capacity degradation caused by the extreme volume expansion, dramatic structure pulverization, and the loss of electronic connection during continuously repeated lithiation/delithiation processes [6,11]. Multicomponent metal oxides, such as $ZnMn_2O_4$ [12] and $ZnCo_2O_4$ [13] usually

**Foundation item:** Project (2019zzts502) supported by the Fundamental Research Funds for the Central Universities of Central South University, China; Project (2018GK4001) supported by the Scientific and Technological Breakthrough and Major Achievements Transformation of Strategic Emerging Industries of Hunan Province, China
**Corresponding author:** Jing ZHAN, Tel: +86-13975147556, E-mail: zhanjing@csu.edu.cn;
Qi-hou LI, E-mail: li_qihou@126.com
DOI: 10.1016/S1003-6326(20)65371-7

exhibit better electrochemical properties than single-component metal oxides on account of their abundant composition and synergistic effects among various metals [14,15].

Especially, mullite-type compound $Bi_2Mn_4O_{10}$ with a considerable theoretical specific capacity of 873 mA·h/g has been investigated as an anode material for advanced Li-ion battery systems. SONG et al [16] prepared a $Bi_2Mn_4O_{10}$ anode material via the sol−gel method, which displayed a high reversible specific capacity of 711.6 mA·h/g at 60 mA/g. Furthermore, our group synthesized $Bi_2Mn_4O_{10}$ nanoparticles, which maintained a stable reversible specific capacity of 402.3 mA·h/g after 50 cycles at 0.2*C* [17]. It is essential to improve cycling lifespan and rate performances of $Bi_2Mn_4O_{10}$. Downsizing the bulk material to nanoscale and integrating with highly conductive and excellent chemical stable carbon were considered as one of the most effective strategies for LIBs to circumvent capacity fading, inferior rate performance, and poor cyclic durability [18,19]. Reducing the size of particles can not only tailor the properties of surface interface and expose numerous active sites, but also ensure the adequate diffusion of electrolyte and ions [20]. As known, the carbon-based materials not only have high conductivity and stability but also can provide a larger reaction space to relieve the volume change during the continuous insertion/extraction of $Li^+$, thereby reliably inhibiting the pulverization of electrode materials. In addition, doping elemental nitrogen (N) into the conductive carbon matrix is propitious to create extensive defects and active sites without causing lattice mismatch, which significantly strengthens the electrical conductivity and wettability, thus accelerating the faster transfer of ions and the highly reversible conversion reaction [21]. Hence, the economical and efficient preparation of $Bi_2Mn_4O_{10}$/C anode composites using carbon materials with excellent electrochemical properties is of great significance for improving the cycle stability, lithium storage capacity, and rate performance of $Bi_2Mn_4O_{10}$ in portable electronic equipment and electric vehicles.

In this work, the N-doped Ketjen black (ECP-N) was prepared by a low-cost calcination reduction method. Subsequently, the $Bi_2Mn_4O_{10}$/ECP-N nanocomposites were prepared via a simple wet ball milling method. Most significantly, the $Bi_2Mn_4O_{10}$/ECP-N composites serving as anodes for LIBs demonstrated higher cycling stability than bare $Bi_2Mn_4O_{10}$. An attractive specific capacity of 576.2 mA·h/g was obtained at 0.2*C* after 100 cycles with prominent retention of 75%, while bare $Bi_2Mn_4O_{10}$ only conveyed 169.5 mA·h/g with inferior retention of 27%. The ECP with N dopants not only suppresses the aggregation of $Bi_2Mn_4O_{10}$ nanoparticles but also offers substantial defect sites to enhance ions transport and electronic conductivity.

## 2 Experimental

### 2.1 Material synthesis

All chemical reagents were used directly to prepare target samples without further purification. $Bi_2Mn_4O_{10}$/ECP-N material was synthesized via a typical method. Firstly, the preparation of $Bi_2Mn_4O_{10}$ powders was given in our previous report [17]. In this work, the ball milling time for preparing $Bi_2Mn_4O_{10}$ powders was 18 h. ECP-N was synthesized via calcining Ketjen black (ECP600JD, Triquo Chemical Technology Co., Ltd.) at 800 °C under $NH_3$ for 10 h. Then, 20 g $Bi_2Mn_4O_{10}$ powders and 2 g ECP-N were added into a 250 mL ball mill tank for ball milling for 8 h to obtain the precursor, which was calcined at 300 °C in air for 3 h with a heating ramp of 2 °C/min, marked as $Bi_2Mn_4O_{10}$/ECP-N.

### 2.2 Material characterization

The crystallographic structures of $Bi_2Mn_4O_{10}$ and $Bi_2Mn_4O_{10}$/ECP-N were investigated by an X-ray powder diffractometer (XRD, Rigaku−TTRIII) allocated with Cu $K_\alpha$ at 8 (°)/min. The morphologies of the as-prepared materials were observed by the scanning electron microscope (SEM, JSM−6360LV) and the transmission electron microscope (TEM, TEM, JEM−2100F). The Brunauer−Emmett−Teller (BET) specific surface areas and Barrett–Joyner–Halenda (BJH) pore size distribution of as-prepared materials were calculated according to $N_2$ adsorption isotherms (ASAP2020). X-ray photoelectron spectroscopy

analysis (XPS, Kratos Axis Ultra DLD) was used to testify the chemical composition of $Bi_2Mn_4O_{10}$/ECP-N.

### 2.3 Electrochemical test

In this work, the 2025-type coin cells were employed to measure the electrochemical properties of as-prepared materials. The assembling of cells was performed in the glove box filled with high purity argon, using lithium foil as the counter electrode. 1 mol/L $LiPF_6$ in a mixture of ethylene carbonate (EC), dimethyl carbonate (DMC), and diethyl carbonate (DEC) with a volume ratio of 1:1:1 was employed as the electrolyte. Moreover, porous polypropylene membranes were applied as the separator. For obtaining the working electrode, the as-prepared electroactive materials were mixed with conductive carbon and polyvinylidene fluoride (PVDF) at a mass ratio of 7:2:1. The mixture was homogeneously painted on the copper foil and dried in a vacuum oven for 12 h at 80 °C, which was further cut into wafers with a diameter of 12.0 mm. The final mass of electroactive materials was approximately 1.2 mg/cm. The galvanostatic charge/discharge cycling characterization was performed on LANHE cell tester (CT2001A, Wuhan, China) between 0.05 and 3.0 V at room temperature. The electrochemical workstation (CHI 760e) was used to obtain the cyclic voltammogram (CV) between 0.05 and 3.0 V at a scan rate of 0.1 mV/s. Electrochemical impedance spectroscopy (EIS) measurements were also carried out on a CHI 760e system in the frequency range of 0.01−100000 Hz.

## 3 Result and discussion

### 3.1 Phase structure

The crystalline nature of the as-prepared $Bi_2Mn_4O_{10}$ nanoparticles and $Bi_2Mn_4O_{10}$/ECP-N composites was investigated by XRD and the corresponding results were depicted in Fig. 1. As can be seen from Fig. 1, the ball-milled $Bi_2Mn_4O_{10}$ nanoparticles and $Bi_2Mn_4O_{10}$/ECP-N composites exhibit nearly the same XRD patterns, which perfectly match with the pure $Bi_2Mn_4O_{10}$ phase (JCPDS No. 27−0048). However, there is a diffraction peak of $Bi_2O_3$ in Fig. 1(b), which might be attributable to the relatively short milling time. The bismuth and manganese cannot be mixed uniformly, resulting in the existence of the $Bi_2O_3$ phase. After the $Bi_2Mn_4O_{10}$ powders and ECP-N were mixed by ball milling for 8 h, no peak of $Bi_2O_3$ was detected, indicating the higher purity of the as-obtained $Bi_2Mn_4O_{10}$/ECP-N. Moreover, the peak intensities of $Bi_2Mn_4O_{10}$/ECP-N composite become weaker than those of $Bi_2Mn_4O_{10}$, which indicates that the crystallinity of different crystal faces declines and the grain size is smaller after ball milling with ECP-N. The interplanar spacing ($d$) and grains size ($D_{hkl}$) can be estimated through the Bragg equation $2d\sin\theta=n\lambda$ ($n$ is the diffraction series, $\theta$ is the angle of incidence on a crystal plane and $\lambda$ is the wavelength), and Scherrer equation $D_{hkl}=K\lambda/(\beta\cos\theta)$ ($K$=0.89, $\lambda$=0.154 nm, and $\beta$ is the full width at half-maximum (FWHM)). Corresponding results are listed in Table 1. After ball milling with ECP-N, the interplanar spacing and grain size of $Bi_2Mn_4O_{10}$ nanoparticles decreased obviously, which were of great significance to increase the specific surface area of the sample and release substantial active sites for $Li^+$ storage. In addition, no obvious peak of ECP-N was detected on account of the higher peak

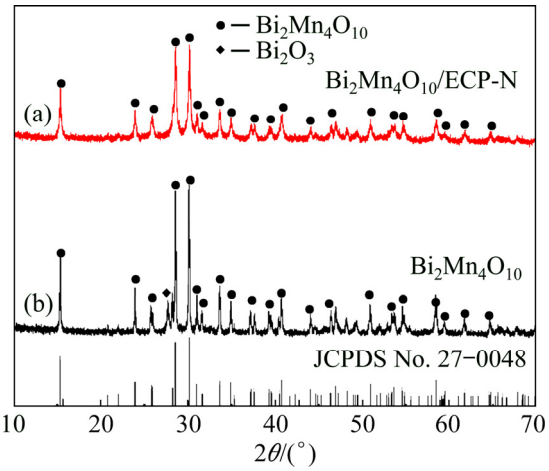


**Fig. 1** XRD patterns of as-synthesized $Bi_2Mn_4O_{10}$/ECP-N (a) and bare $Bi_2Mn_4O_{10}$ (b)

**Table 1** Structural parameters of $Bi_2Mn_4O_{10}$ and $Bi_2Mn_4O_{10}$/ECP-N determined from XRD Rietveld refinement

| Sample | $2\theta$/(°) | $\beta$/rad | $D_{hkl}$/nm | $d_{(121)}$/nm |
|---|---|---|---|---|
| $Bi_2Mn_4O_{10}$ | 28.568 | 0.0026 | 52.71 | 0.3121 |
| $Bi_2Mn_4O_{10}$/ECP-N | 28.586 | 0.0047 | 29.16 | 0.3119 |

intensity of $Bi_2Mn_4O_{10}$, indicating that the low content of ECP-N had no obvious effect on the crystallization behavior of the $Bi_2Mn_4O_{10}$.

### 3.2 SEM and TEM morphologies

The typical SEM and TEM images of as-synthesized materials were revealed in Fig. 2. As shown in Fig. 2(a), the $Bi_2Mn_4O_{10}$/ECP-N composites were mainly composed of well-developed nanoparticles with particle sizes ranging from one hundred to several hundred nanometers. The morphology of $Bi_2Mn_4O_{10}$/ECP-N nanoparticles demonstrated uniform distribution because the $Bi_2Mn_4O_{10}$/ECP-N nanocrystals could be well separated and stabilized by the doped carbon matrix. Figure 2(c) displayed that the fine lattice fringes of $Bi_2Mn_4O_{10}$/ECP-N nanoparticles with an interplanar spacing of approximately 0.265 nm, which corresponded to the (130) crystalline plane of the $Bi_2Mn_4O_{10}$ phase. This result further demonstrated the $Bi_2Mn_4O_{10}$/ECP-N nanocrystals with superior crystallization and purity. As can be seen from the SEM and TEM images of ECP-N in Figs. 2(b, d), ECP-N showed a nanoparticle structure with the particle size distribution between tens of nanometers and hundreds of nanometers, which could be conducive to uniform doping during the ball-milling.

To evidence elements distribution in $Bi_2Mn_4O_{10}$/ECP-N composites, the element mapping was measured via the energy-dispersive spectroscopy (EDS), as demonstrated in Fig. 3. The elemental mapping of $Bi_2Mn_4O_{10}$/ECP-N nanoparticles indicated the existence of Bi, Mn, N, C and O elements (Figs. 3(a−f)). The uniform distribution of element C will improve more abundant reaction area and strengthen the electrical conductivity of $Bi_2Mn_4O_{10}$, and the uniform distribution of element N provides substantial defects and active sites, which will improve the wettability of $Bi_2Mn_4O_{10}$ in the electrolyte and the electrochemical properties of the $Bi_2Mn_4O_{10}$ anode material.

In particular, the interaction among $Li^+$ and $Bi_2Mn_4O_{10}$, ECP, N-ECP was also measured via the contact angle test. As shown in Figs. 3(g−i), the three electrodes with $Bi_2Mn_4O_{10}$, ECP, and ECP-N

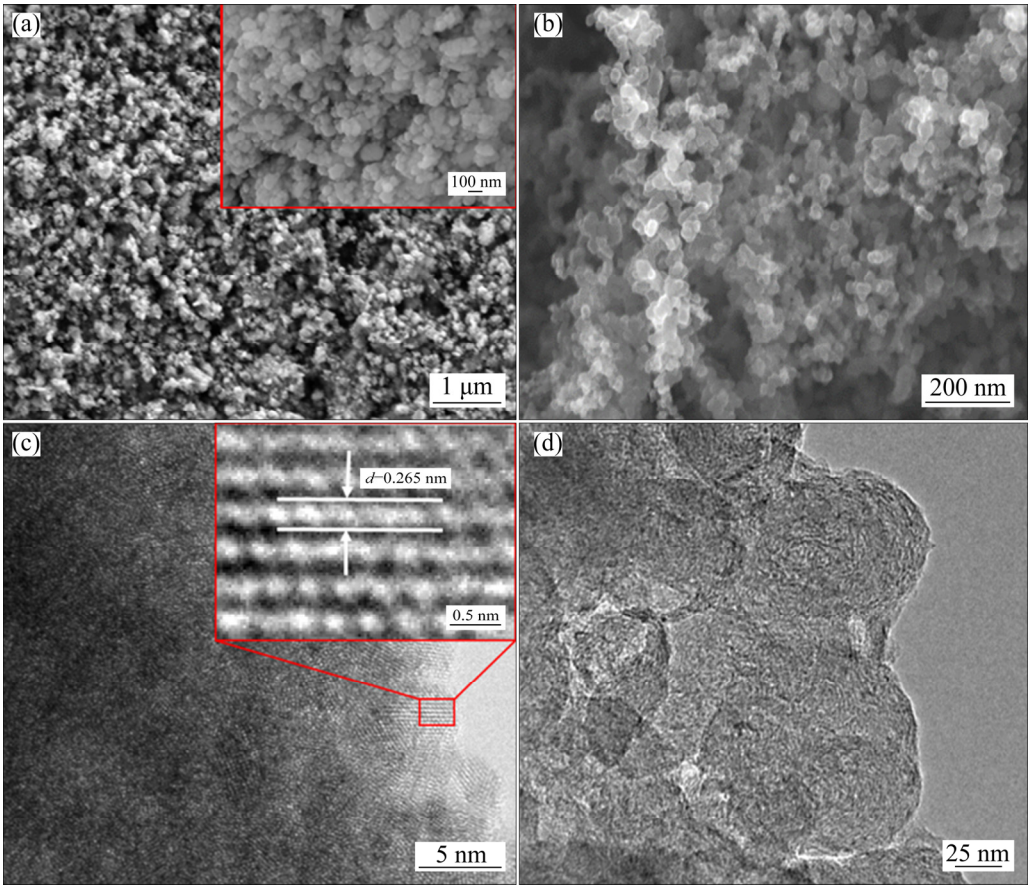


**Fig. 2** Low and high magnification SEM images of $Bi_2Mn_4O_{10}$/ECP-N (a), SEM image of ECP-N (b), high-resolution TEM image of $Bi_2Mn_4O_{10}$/ECP-N (c) and TEM image of ECP-N (d)

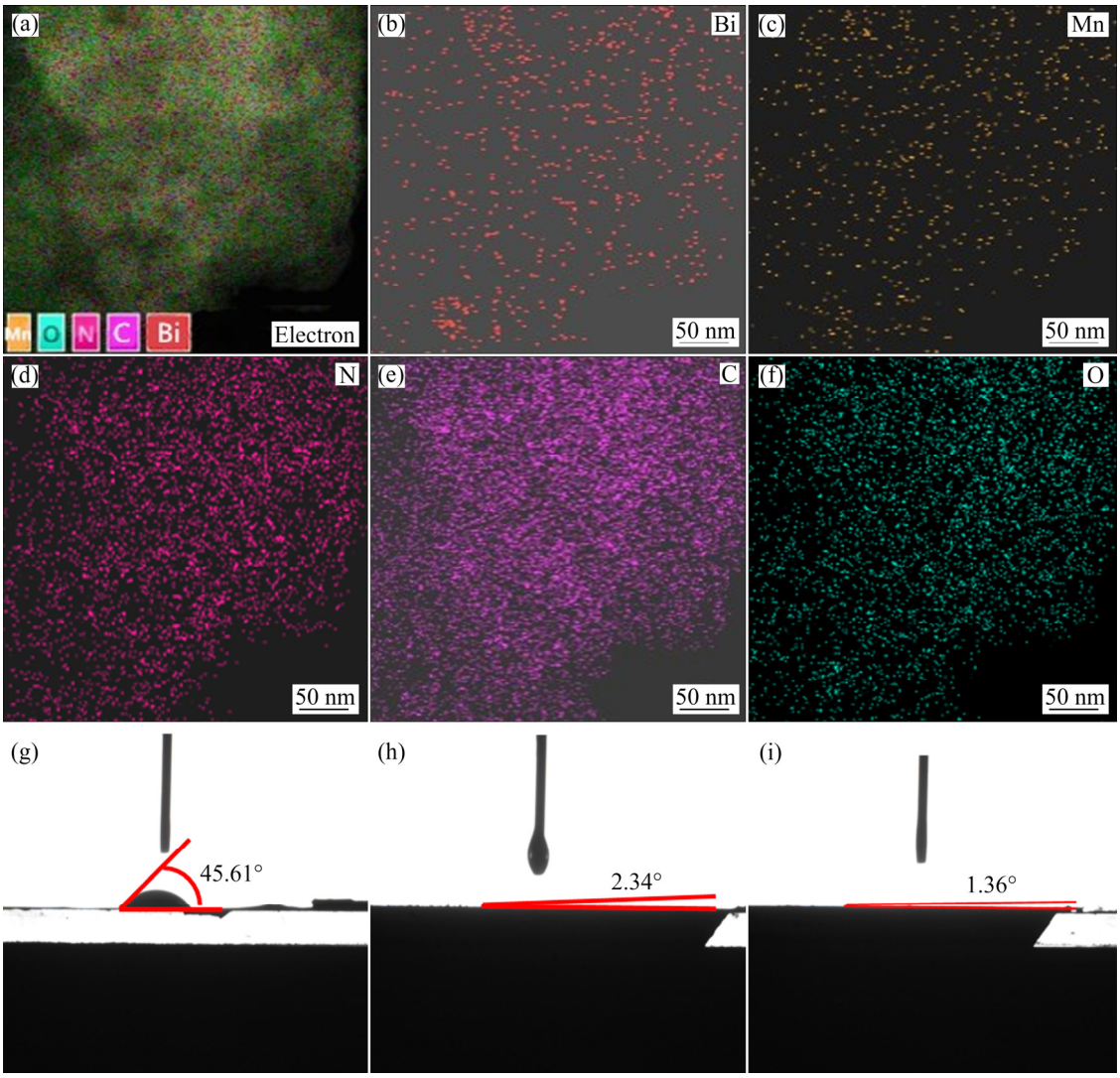


**Fig. 3** EDS image of $Bi_2Mn_4O_{10}$/ECP-N (a), corresponding element mapping of Bi (b), Mn (c), N (d), C (e), O (f) and comparison of interface contact angle of $Bi_2Mn_4O_{10}$ (g), ECP (h) and ECP-N (i)

were adopted to characterize the contact angle, respectively, which used the same electrolytes (1 mol/L $LiPF_6$ in a mixture of EC, DMC and DEC (1:1:1, volume ratio)). As shown in Fig. 3(i), ECP-N electrode manifested minimum contact angle of 1.36°, which is smaller than that on the $Bi_2Mn_4O_{10}$ electrode (45.61°, Fig. 3(g)) and ECP electrode (2.34°, Fig. 3(h)), indicating good wettability for electrolyte after being N-doped. The enhanced affinity with electrolyte would promote $Li^+$ transmission, thus increasing the lithium-ion diffusion rate on the surface of the electrode [22], which could be conducive to the improvement of the cyclicity and rate performance.

### 3.3 $N_2$ adsorption/desorption isotherms

Generally, the specific surface area, total pore volume, and pore diameter have significant impact on the electrochemical performance of the electroactive materials, thus typical $N_2$ adsorption/desorption isotherm measurements were implemented to characterize the porous features and textural properties of the as-prepared $Bi_2Mn_4O_{10}$/ECP-N and $Bi_2Mn_4O_{10}$ samples more clearly. As shown in Fig. 4, all $N_2$ isotherms could be classified as typical type-IV characteristics with a type-H1 hysteresis loop [23,24], revealing mesoporous characteristics. Their BET specific surface area and total pore volume were computed to be 33.72 $m^2/g$ and 0.1538 $cm^3/g$ for $Bi_2Mn_4O_{10}$/ECP-N, 11.87 $m^2/g$ and 0.0232 $cm^3/g$ for $Bi_2Mn_4O_{10}$, respectively. The relatively large surface area and total pore volume of $Bi_2Mn_4O_{10}$/ECP-N were beneficial to providing the electrochemical uptake

and release of $Li^+$ ions, and favoring enough room to accommodate volume expansion/ contraction during continuous cycling. Furthermore, the mesoporous characteristics could also be further testified by the Barrett−Joyner−Halenda (BJH) pore-size distribution (PSD) in the insets of Figs. 4(a, b), the pore distributions of $Bi_2Mn_4O_{10}$/ECP-N and $Bi_2Mn_4O_{10}$ were mostly in the range of 2−20 nm, and their average pore sizes were approximately 18.24 and 7.83 nm respectively, which strongly demonstrated that the $Bi_2Mn_4O_{10}$/ECP-N contained a great number of mesoporous architectures. Indeed, the abundant mesoporous configuration not only promotes the contact between electroactive materials and electrolytes but also provides sufficient surfaces/interfaces to boost charge transfer and shorten path length of ion diffusion, thus strongly increasing the electrochemical performance of samples [23].

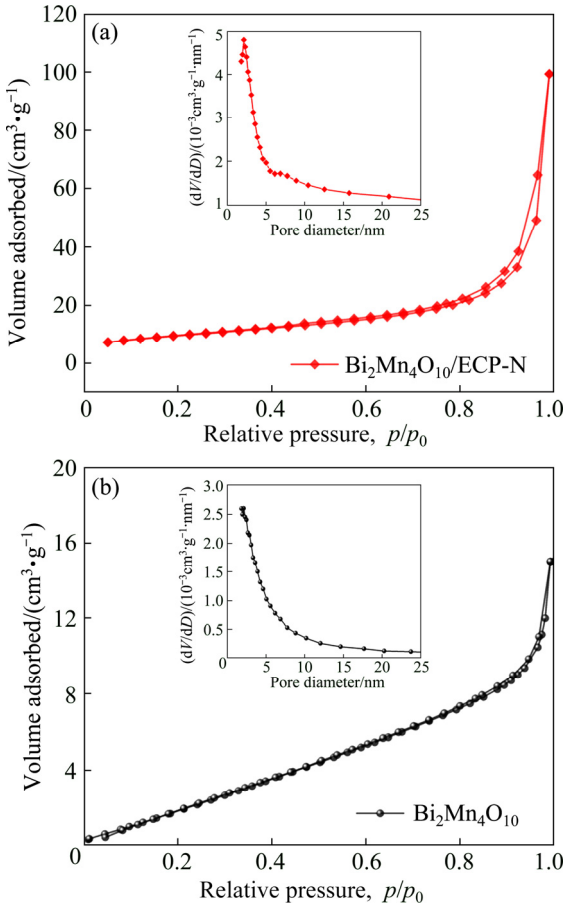


**Fig. 4** $N_2$ adsorption/desorption isotherms of $Bi_2Mn_4O_{10}$/ECP-N (a) and $Bi_2Mn_4O_{10}$ (b) (Insets in (a, b) show corresponding BJH pore size distribution plots)

### 3.4 XPS spectra

The XPS was employed to characterize the chemical elements and the surface chemical valence states. The as-obtained XPS data and typically fitted curves by using the Gaussian fitting method were collected and shown in Fig. 5. The main peaks of Bi 4f, C 1s, O 1s, and Mn 2p were delivered in the survey spectrum of $Bi_2Mn_4O_{10}$/ECP-N in Fig. 5(a), and another weak peak was situated at about 398 eV, which corresponded to the N 1s. As shown in the high-resolution spectrum of Bi 4f (Fig. 5(b)), the binding energies situated at 160.2 and 165.5 eV were contributed to Bi $4f_{5/2}$ and Bi $4f_{7/2}$, respectively [15,25]. As shown in Fig. 5(c), the high-resolution spectrum of Mn 2p exhibited two the characteristic peaks at 641.3 and 652.9 eV, which corresponded to Mn $2p_{3/2}$ and Mn $2p_{1/2}$, respectively. Moreover, the spectrum of Mn 2p could be separated into four peaks, in which 641.2 and 652.9 eV could characterize the existence of $Mn^{3+}$, and the other two peaks at 642.5 and 654.1 eV could be assigned to $Mn^{4+}$ species [23]. According to the high-resolution spectra of C 1s in Fig. 5(d), three peaks at 284.4, 285.6 and 288.6 eV were attributed to C—C, C—N, and C═O groups, which indicated that N atoms had been doped into the electroactive materials [26]. The existence of N species was further testified by N 1s peak in Fig. 5(e). The peaks located at 398.8, 399.6 and 401.4 eV could be assigned to pyridinic-N, pyrrolic-N and graphitic-N, respectively [22,27]. The total content of N was approximately 1.9%, which could enhance lithium-storage capability.

### 3.5 Electrocatalytic behavior

Subsequently, the $Bi_2Mn_4O_{10}$/ECP-N was configured as an anode in a half cell, in which metallic lithium foil was utilized as the counter electrode, highlighting the application prospects of the material for high-performance LIBs and evaluating its electrochemical lithium-storage performance. The lithium-ion storage mechanism of $Bi_2Mn_4O_{10}$/ECP-N composites was preliminarily investigated using cyclic voltammetry in the voltage range of 0.05−3.0 V (vs $Li^+$/Li) at a scan rate of 0.1 mV/s. As shown in Fig. 6(a), the CV curves displayed multipeak characteristics, indicating that the reaction between $Li^+$ and the $Bi_2Mn_4O_{10}$/ECP-N was multistep. During the first negative scan, two irreversible cathodic peaks at about 1.19 and 0.73 V could be attributed to the decomposition of the electrolyte and the reduction

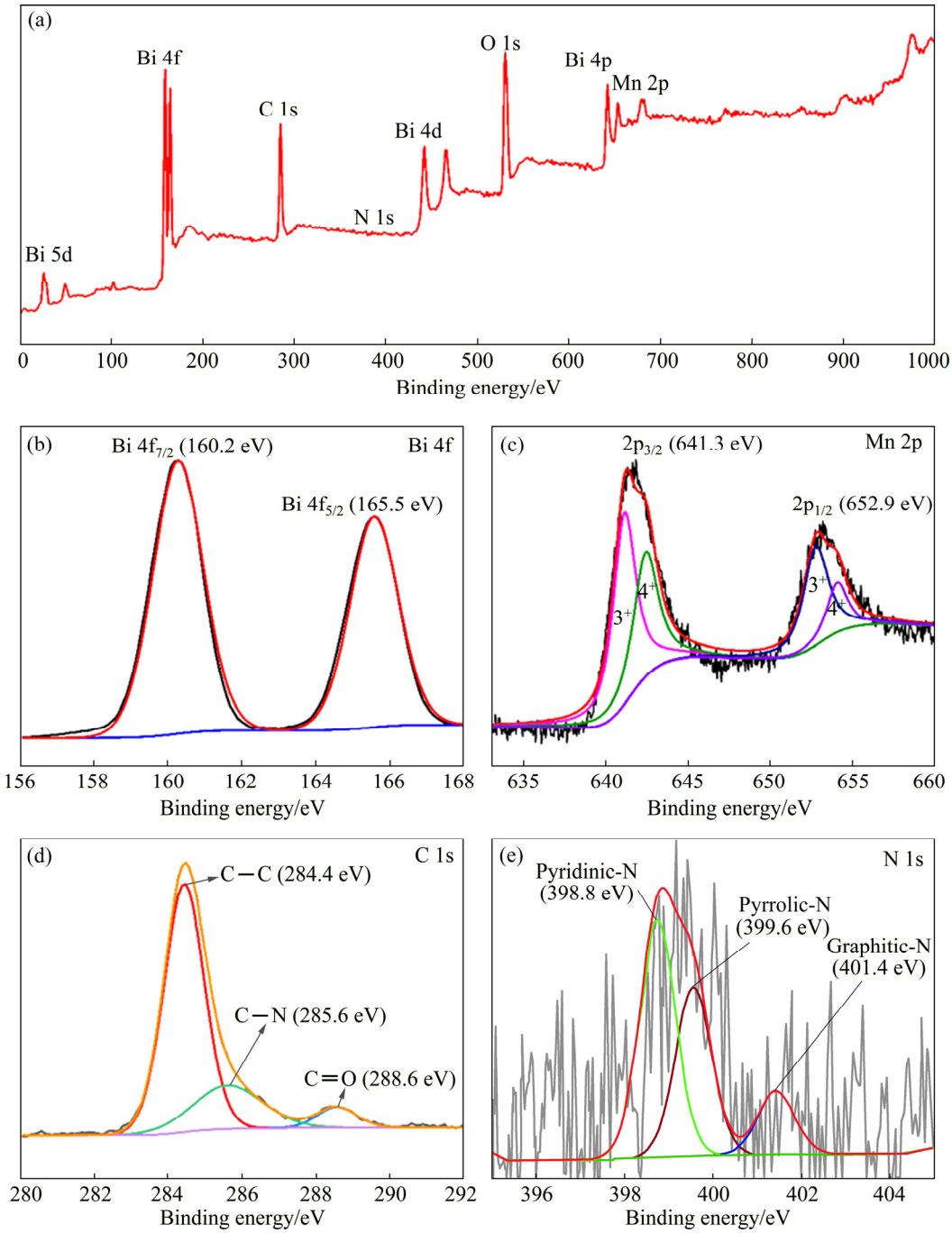


**Fig. 5** Full XPS spectrum of $Bi_2Mn_4O_{10}$/ECP-N (a), high-resolution XPS spectrum of Bi 4f (b), Mn 2p (c), C 1s (d) and N 1s (e)

of $Mn^{3+}$, $Mn^{4+}$ and $Bi^{3+}$ to $Mn^0$ and $Bi^0$ with the production of $Li_2O$, respectively [28,29]. The cathodic peak at around 0.38 V could be associated with the formation of SEI films and alloying reaction between Bi and Li, which could be considered as a multistep alloying reaction. However, the broad peak was divided into two small peaks at ~1.37 and ~1.06 V in subsequent cycles, which corresponded to the reduction of BiO to metallic Bi and MnO to metallic Mn, respectively [28,29]. During the positive scan, a strong anodic peak at around 1.12 V could be related to the dealloying processes of $Li_3Bi$. Furthermore, two broad anodic peaks at about 1.4 and 1.7 V might have originated from the oxidation of Bi and Mn metal clusters. The aforementioned main reactions were shown in Table 2. From the CV curves, it was obvious that the reduction peaks and

oxidation peaks exhibited apparent overlapped characteristics, which verified that the electrode exhibited excellent reversibility and stability during the electrochemical reaction.

As illustrated in Fig. 6(b), the initial discharge specific capacity and charge specific capacity were 1207 and 823 mA·h/g, delivering Coulombic efficiency of 68%, the initial irreversible capacity loss could be attributed to the irreversible redox reaction and the formation of SEI layer on the anode electrode [30]. The formation of SEI layer is indispensable to conversion-type anode materials

**Table 2** Chemical reactions during charge/discharge processes

| Process | Chemical equation |
|---|---|
| Discharge | $Bi_2Mn_4O_{10}+20Li^++20e\rightarrow 2Bi+4Mn+10Li_2O$ |
| | $2Bi+6Li^++6e\rightarrow 4Li^++2LiBi+4e\rightarrow 2Li_3Bi$ |
| | $2BiO+4Li^++4e\rightarrow 2Bi+2Li_2O$ |
| | $4MnO+8Li^++8e\rightarrow 4Mn+4Li_2O$ |
| Charge | $2Li_3Bi\rightarrow 4Li^++2LiBi+4e\rightarrow 2Bi+6Li^++6e$ |
| | $2Bi+2Li_2O\rightarrow 2BiO+4Li^++4e$ |
| | $4Mn+4Li_2O\rightarrow 4MnO+8Li^++8e$ |

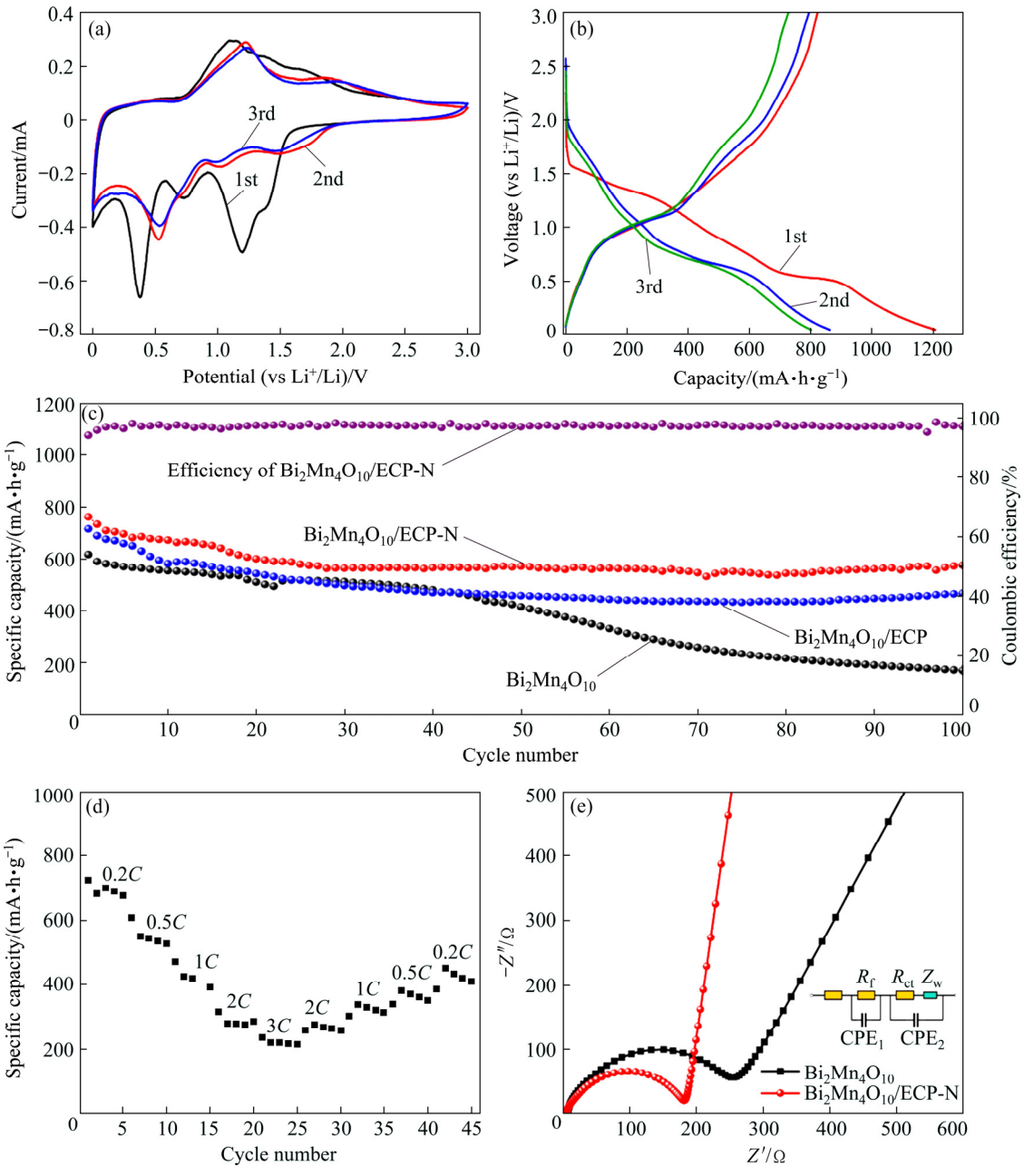


**Fig. 6** CV curves of $Bi_2Mn_4O_{10}$/ECP-N (a), charge/discharge curves of $Bi_2Mn_4O_{10}$/ECP-N (b), cycling performance of $Bi_2Mn_4O_{10}$, $Bi_2Mn_4O_{10}$/ECP and $Bi_2Mn_4O_{10}$/ECP-N at 0.2*C* (1*C*=800 mA/g) (c), rate performance curve of $Bi_2Mn_4O_{10}$/ECP-N (d) and EIS Nyquist curves of $Bi_2Mn_4O_{10}$ and $Bi_2Mn_4O_{10}$/ECP-N (e)

for large volume expansion [31]. Expectably, the stable redox processes could be obtained after the first cycle, resulting in high capacity retention, which could be clearly demonstrated in Fig. 6(c). As we could see the cycle performance at 0.2*C* in Fig. 6(c), it was obvious that the $Bi_2Mn_4O_{10}$/ECP-N displayed a higher discharge specific capacity than the $Bi_2Mn_4O_{10}$/ECP and $Bi_2Mn_4O_{10}$. The specific capacity of $Bi_2Mn_4O_{10}$/ECP-N showed a slight decrease and stabilized at 576.2 mA·h/g after 100 cycles, while the $Bi_2Mn_4O_{10}$/ECP and $Bi_2Mn_4O_{10}$ only demonstrated the specific capacity of 467.3 and 169.5 mA·h/g, respectively. It was obvious that the introduction of ECP-N could significantly strengthen the cycle stability, which could be ascribed to the protection of layered ECP-N for structural change during long-term continuous charge and discharge processes, and could be related to the better wettability for electrolyte after being nitrogen-doped. Figure 6(d) indicated that the $Bi_2Mn_4O_{10}$/ECP-N composite showed superior rate performance and delivered reversible capacities of 723.1, 607.4, 470.5, 314.6 and 236.1 mA·h/g, at the current densities of 0.2*C*, 0.5*C*, 1*C*, 2*C* and 3*C*, respectively. These results are more satisfactory than previous work of bare $Bi_2Mn_4O_{10}$ [17]. The electrochemical performance based on other Bi−M−O compounds anode materials for lithium−ion batteries was summarized in Table 3.

**Table 3** Electrochemical performance comparison of $Bi_2Mn_4O_{10}$/ECP-N with other reported Bi−M−O compound anode materials for lithium-ion batteries

| Material | Cyclability/ ($mA·h·g^{-1}$) | Rate capability/ ($mA·h·g^{-1}$) | Resource |
|---|---|---|---|
| $Bi_2Mn_4O_{10}$/ ECP-N | 576.2 at 1.6 A/g after 100 cycles | 236.1at 2.4 A/g | This work |
| $Bi_2Mn_4O_{10}$ | 402.3 at 1.6 A/g after 50 cycles | 223 at 1.6 A/g | [17] |
| $Bi_2Mn_4O_{10}$/C | 846 at 0.6 A/g after 300 cycles | 504 at 1.2 A/g | [16] |
| $Bi_5Nb_3O_{15}$ | 267 at 0.1 A/g after 100 cycles | 170 at 0.8 A/g | [32] |
| $Bi_5Nb_3O_{15}$@C | 212.06 at 0.1 A/g after 100 cycles | 173.52 at 0.7 A/g | [33] |
| $BiNbO_4$ | 60 at 0.1 A/g after 700 cycles | 89 at 0.7 A/g | [34] |

The heightened cyclic persistence and rate performance of $Bi_2Mn_4O_{10}$/ECP-N could be closely related to their excellent conductivity owing to the existence of ECP-N, which could be evidenced by EIS characterization. The fitted Nyquist plots and relative equivalent circuit model were displayed in Fig. 6(e). The semicircle in high-medium frequency was characterized as the charge transfer resistance ($R_{ct}$), which was ascribed to the electrochemical reactions between the interface of electrolyte and electrodes, the oblique line in low-frequency regions reflected Warburg impedance ($Z_w$) for $Li^+$ diffusion [35,36]. In addition, $R_e$ and $R_f$ were ascribed to the resistances of the solvent electrolyte and SEI films, respectively. The resistance value of $R_{ct}+R_e+R_f$ for the $Bi_2Mn_4O_{10}$/ECP-N (185.808 Ω) was smaller than that of $Bi_2Mn_4O_{10}$ (252.971 Ω), suggesting that $Bi_2Mn_4O_{10}$/ECP-N composite anode material possessed a faster charge transfer than the bare $Bi_2Mn_4O_{10}$ anode. Additionally, the linear slope of $Bi_2Mn_4O_{10}$/ECP-N composite in low-frequency region was larger than that of bare $Bi_2Mn_4O_{10}$, indicating the $Li^+$ diffusion rate could be increased by using $Bi_2Mn_4O_{10}$/ECP-N composite anode. Furthermore, the $Li^+$ diffusion coefficient ($D_{Li^+}$) could be estimated from the low-frequency regions by the following formula: $D_{Li^+}=0.5(RT)^2/(An_1^2F^2C\sigma)^2$, where $R$ is the mole gas constant and $R$=8.314 J/(mol·K), $T$ is the thermodynamic temperature and $T$=298 K, electrode surface area $A$=1.13 $cm^2$, $F$ is the Faraday constant and $F$=96500 C/mol, the concentration of $Li^+$ $C$=0.001 mol/$cm^3$, $n_1$ is the electronic transfer number, and $\sigma$ is the Warburg coefficient resulting from $Z'=R_{ct}+R_e+R_f+\sigma\omega^{-1/2}$, $\omega=2\pi f$ ($Z'$, $\omega$ and $f$ represented the real impedance, angular frequency and frequency, respectively). The EIS fitting statistic values and $Li^+$ diffusion were presented in Table 4. The calculated $D_{Li^+}$ value of $Bi_2Mn_4O_{10}$/ECP-N ($8.54\times10^{-13}$ $cm^2/s$) is much higher than that of pristine $Bi_2Mn_4O_{10}$ ($9.71\times10^{-14}$ $cm^2/s$), revealing

**Table 4** EIS fitting statistic values and $Li^+$ diffusion coefficient

| Sample | $R_e$/Ω | $R_f$/Ω | $R_{ct}$/Ω | $\sigma$ | $D_{Li^+}$/ ($cm^2·s^{-1}$) |
|---|---|---|---|---|---|
| $Bi_2Mn_4O_{10}$ | 6.821 | 35.95 | 210.2 | 534.18 | $9.71\times10^{-14}$ |
| $Bi_2Mn_4O_{10}$/ ECP-N | 4.918 | 5.09 | 175.8 | 180.16 | $8.54\times10^{-13}$ |

the high $Li^+$ diffusion coefficient and excellent reaction kinetics after the introduction of ECP-N. $Bi_2Mn_4O_{10}$/ECP-N illuminated smaller charge transfer resistance and Warburg impedance than bare $Bi_2Mn_4O_{10}$, reflecting that the introduction of ECP-N can not only advance $Li^+$ diffusion and enhance the conductivity of the electroactive materials but also reduce the resistance of the charge transfer and enhance the reaction kinetics. Therefore, $Bi_2Mn_4O_{10}$/ECP-N composite anode exhibited a superior cycle and rate performance.

## 4 Conclusions

(1) The high-purity mesoporous architecture $Bi_2Mn_4O_{10}$/ECP-N composite anode material with uniform distribution of C and N elements was designed via a convenient wet ball-milling method.

(2) Benefiting from the ECP-N layers, the $Bi_2Mn_4O_{10}$/ECP-N composite anode demonstrates a high capacity of 576.2 mA·h/g after 100 cycles at 0.2*C* with a capacity retention of 75%, which is much higher than that of bare $Bi_2Mn_4O_{10}$ (only 27%). Even at 3*C*, a superior rate capacity of 236.1 mA·h/g is retained.

(3) The N dopants make ECP have good wettability and electronic affinity, which can be beneficial to promoting the electronic conductivity of $Bi_2Mn_4O_{10}$/ECP-N and enhance kinetics. In addition, using ECP-N as the buffer layer is a pretty effective technique to mitigate volume expansion and alleviate the rapid capacity decline. This work provides a potential electroactive material for lithium-ion batteries and a design strategy for large-scale synthesizing nanocomposite electrode materials.

## References


[1] CHABI S, PENG C, HU D, ZHU Y Q. Ideal three-dimensional electrode structures for electrochemical energy storage [J]. Advanced Materials, 2014, 26(15): 2440−2445.

[2] PENG Ke, ZHANG Zhi-jian, ZHAO Ze-jun, YANG Chao, TIAN Zhong-liang, LAI Yan-qing. Performance of carbon-coated nano-ZnO prepared by carbonizing gel precursor as anodic material for secondary alkaline Zn batteries [J]. Transactions of Nonferrous Metals Society of China, 2019, 29(10): 2151−2159.

[3] GUO J C, LIU Q, WANG C S, ZACHARIAH M R. Interdispersed amorphous $MnO_x$−carbon nanocomposites with superior electrochemical performance as lithium-storage material [J]. Advanced Functional Materials, 2012, 22(4): 803−811.

[4] QIU Yong-cai, XU Gui-liang, YAN Ke-you, SUN Hui, XIAO Jun-wu, YANG Shi-he, SUN Shi-gang, JIN Li-min, DENG Hong. Morphology-conserved transformation: Synthesis of hierarchical mesoporous nanostructures of $Mn_2O_3$ and the nanostructural effects on Li-ion insertion/deinsertion properties [J]. Journal of Materials Chemistry, 2011, 21(17): 6346−6353.

[5] KUNDU M, NG C C A, PETROVYKH D Y, LIU L F. Nickel foam supported mesoporous $MnO_2$ nanosheet arrays with superior lithium storage performance [J]. Chemical Communications, 2013, 49(76): 8459−8461.

[6] REDDY M V, RAO G V S, CHOWDARI B V R. Metal oxides and oxysalts as anode materials for Li ion batteries [J]. Chemical Reviews, 2013, 113(7): 5364−5457.

[7] ZHAO Yang, LIU Ting-ting, XIA Hui, ZHANG Ling, JIANG Jia-xing, SHEN Ming, NI Jiang-feng, GAO Li-jun. Branch-structured $Bi_2S_3$−CNT hybrids with improved lithium storage capability [J]. Journal of Materials Chemistry A, 2014, 2(34): 13854−13858.

[8] CHEN Jun, ZHAN Jing, LI Qi-hou. Exploration and crystal phase engineering from bismuthinite ore to visible-light responsive photocatalyst of $Bi_2O_3$ [J]. Journal of Environmental Chemical Engineering, 2019, 7(5): 103375.

[9] CHEN Jun, ZHAN Jing, ZHANG Yu-meng, TANG Yi-wei. Construction of a novel $ZnCo_2O_4$/$Bi_2O_3$ heterojunction photocatalyst with enhanced visible light photocatalytic activity [J]. Chinese Chemical Letters, 2019, 30(3): 735−738.

[10] DENG Zhuo, LIU Ting-ting, CHEN Tao, JIANG Jia-xiang, YANG Wan-li, GUO Jun, ZHAO Jian-qing, WANG Hai-bo, GAO Li-jun. Enhanced electrochemical performances of $Bi_2O_3$/rGO nanocomposite via chemical bonding as anode materials for lithium ion batteries [J]. ACS Applied Materials & Interfaces, 2017, 9(14): 12469−12477.

[11] CABANA J, MONCONDUIT L, LARCHER D, PALACIN M R. Beyond intercalation-based Li-ion batteries: The state of the art and challenges of electrode materials reacting through conversion reactions [J]. Advanced Materials, 2010, 22(35): E170−E192.

[12] GAO Qi-li, YUAN Zhao-xiao, DONG Lin-xi, WANG Gao-feng, YU Xue-bin. Reduced graphene oxide wrapped $ZnMn_2O_4$/carbon nanofibers for long-life lithium-ion batteries [J]. Electrochimica Acta, 2018, 270: 417−425.

[13] ZHAO Rui-zheng, LI Qun, WANG Cheng-xiang, YIN Long-wei. Highly ordered mesoporous spinel $ZnCo_2O_4$ as a high-performance anode material for lithium-ion batteries [J]. Electrochimica Acta, 2016, 197: 58−67.

[14] SHEN Lai-fa, YU Le, YU Xin-yao, ZHANG Xiao-gang, LOU Xiong-wen. Self-templated formation of uniform $NiCo_2O_4$ hollow spheres with complex interior structures for lithium-ion batteries and supercapacitors [J]. Angewandte Chemie: International Edition, 2015, 54(6): 1868−1872.

[15] ZHANG Yang, ZHAO Gang-gang, GE Peng, WU Tian-jing, LI Lin, CAI Peng, LIU Cheng, ZOU Guo-qiang, HOU Hong-shuai, JI Xiao-bo. $Bi_2MoO_6$ microsphere with

double-polyaniline layers toward ultrastable lithium energy storage by reinforced structure [J]. Inorganic Chemistry, 2019, 58(9): 6410−6421.

[16] SONG Zi-han, ZHANG Hong-zhang, FENG Kai, WANG Huai-qing, LI Xian-feng, ZHANG Hua-min. $Bi_2Mn_4O_{10}$: A new mullite-type anode material for lithium-ion batteries [J]. Dalton Transactions, 2018, 47(23): 7739−7746.

[17] ZHAN Jing, LONG Yi-yu. Synthesis of $Bi_2Mn_4O_{10}$ nanoparticles and its anode properties for LIB [J]. Ceramics International, 2018, 44(12): 14891−14895.

[18] NI Jiang-feng, ZHAO Yang, LIU Ting-ting, ZHENG Hong-he, GAO Li-jun, YAN Cheng-lin, LI Liang. Strongly coupled $Bi_2S_3$@CNT hybrids for robust lithium storage [J]. Advanced Energy Materials, 2014, 4(16): 1400798.

[19] PAN Cheng-chi, YANG Ying-chang, HOU Hong-shuai, JING Ming-jun, ZHU Yi-rong, SONG Wei-xin, JI Xiao-bo. Effect of lithium content on electrochemical property of $Li_{1+x}(Mn_{0.6}Ni_{0.2}Co_{0.2})_{1-x}O_2(0\leq x\leq 0.3)$ composite cathode materials for rechargeable lithium-ion batteries [J]. Transactions of Nonferrous Metals Society of China, 2018, 28(1): 145−150.

[20] GE Peng, LI Si-jie, SHUAI Hong-lei, XU Wei, TIAN Ye, YANG Li, ZOU Guo-qiang, HOU Hong-shuai, JI Xiao-bo. Engineering 1D chain-like architecture with conducting polymer towards ultra-fast and high-capacity energy storage by reinforced pseudo-capacitance [J]. Nano Energy, 2018, 54: 26−38.

[21] XU Chang-fan, ZHANG Kai-wen, ZHANG Da, CHANG Shi-lei, LIANG Feng, YAN Peng-fei, YAO Yao-chun, QU Tao, ZHAN Jing, MA Wen-hui, YANG Bing, DAI Yong-nian, SUN Xue-liang. Reversible hybrid sodium−$CO_2$ batteries with low charging voltage and long-life [J]. Nano Energy, 2020, 68: 104318.

[22] DONG Qing-yuan, HONG Bo, FAN Hai-lin, GAO Chun-hui, HONG Shu, LAI Yan-qing. Electron-rich functional doping carbon host as dendrite-free lithium metal anode [J]. Electrochimica Acta, 2018, 284: 376−381.

[23] ZHANG Long-hai, ZHU Si-qi, CAO Hui, HOU Lin-rui, YUAN Chang-zhou. Hierarchical porous $ZnMn_2O_4$ hollow nanotubes with enhanced lithium storage toward lithium-ion batteries [J]. Chemistry—A European Journal, 2015, 21(30): 10771−10777.

[24] JU Zhi-cheng, MA Guang-yao, ZHAO Yu-long, XING Zheng, QIANG Ying-huai, QIAN Yi-tai. A facile method for synthesis of porous $NiCo_2O_4$ nanorods as a high-performance anode material for Li-ion batteries [J]. Particle & Particle Systems Characterization, 2015, 32(11): 1012−1019.

[25] CHEN Rui, SHEN Zhu-rui, WANG Hu, ZHOU Hui-jing, LIU Yu-ping, DING Da-tong, CHEN Tie-hong. Fabrication of mesh-like bismuth oxide single crystalline nanoflakes and their visible light photocatalytic activity [J]. Journal of Alloys and Compounds, 2011, 509(5): 2588−2596.

[26] HONG Wan-wan, GE Peng, JIANG Yun-ling, YANG Li, TIAN Ye, ZOU Guo-qiang, CAO Xiao-yu, HOU Hong-shuai, JI Xiao-bo. Yolk-shell-structured bismuth@N-doped carbon anode for lithium-ion battery with high volumetric capacity [J]. ACS Applied Materials & Interfaces, 2019, 11(11): 10829−10840.

[27] YUAN Zhao-xia, DONG Lin-xi, GAO Qi-li, HUANG Zhen-guo, WANG Lu-wen, WANG Gao-feng, YU Xue-bin. SnSb alloy nanoparticles embedded in N-doped porous carbon nanofibers as a high-capacity anode material for lithium-ion batteries [J]. Journal of Alloys and Compounds, 2019, 777: 775−783.

[28] ZHENG Yang, ZHOU Teng-fei, ZHAO Xu-dong, PANG Wei-kong, GAO Hong, LI Se-an, ZHOU Zhen, LIU Hua-kun, GUO Zai-ping. Atomic interface engineering and electric-field effect in ultrathin $Bi_2MoO_6$ nanosheets for superior lithium ion storage [J]. Advanced Materials, 2017, 29(26): 1700396.

[29] CHEN Hong-bin, DING Liang-xin, XIAO Kang, DAI Sheng, WANG Su-qing, WANG Hai-hui. Highly ordered $ZnMnO_3$ nanotube arrays from a “self-sacrificial” ZnO template as high-performance electrodes for lithium ion batteries [J]. Journal of Materials Chemistry A, 2016, 4: 16318−16323.

[30] SHARMA Y, SHARMA N, RAO G V S, CHOWDARI B V R. Nanophase $ZnCo_2O_4$ as a high performance anode material for Li-ion batteries [J]. Advanced Functional Materials, 2007, 17(15): 2855−2861.

[31] HU Ling-ling, QU Bai-hua, LI Cheng-chao, CHEN Yue-jiao, MEI Lin, LEI Dan-ni, CHEN Li-bao, LI Qiu-hong, WANG Tai-hong. Facile synthesis of uniform mesoporous $ZnCo_2O_4$ microspheres as a high-performance anode material for Li-ion batteries [J]. Journal of Materials Chemistry A, 2013, 1: 5596−5602.

[32] LI Yu-hang, ZHENG Run-tian, YU Hao-xiang, CHENG Xing, LIU Ting-ting, PENG Na, ZHANG Jun-dong, SHUI Miao, SHU Jie. Fabrication of one-dimensional architecture $Bi_5Nb_3O_{15}$ nanowires by electrospinning for lithium-ion batteries with enhanced electrochemical performance [J]. Electrochimica Acta, 2019, 299: 894−901.

[33] LI Yu-hang, ZHENG Run-tian, YU Hao-xiang, CHENG Xing, ZHU Hao-jie, BAI Ying, LIU Ting-ting, SHUI Miao, SHU Jie. Carbon-coated $Bi_5Nb_3O_{15}$ as anode material in rechargeable batteries for enhanced lithium storage [J]. Ceramics International, 2018, 44(10): 11505−11511.

[34] TANG Guang-xia, ZHU Hao-jie, YU Hao-xiang, CHENG Xing, ZHENG Run-tian, LIU Ting-ting, ZHANG Jun-dong, SHUI Miao, SHU Jie. Ultra-long $BiNbO_4$ nanowires with hierarchical architecture exhibiting reversible lithium storage [J]. Journal of Electroanalytical Chemistry, 2018, 823: 245−252.

[35] ZHOU Qian, LIU Li, HUANG Zhi-feng, YI Ling-guang, WANG Xian-you, CAO Guo-zhong. $Co_3S_4$@polyaniline nanotubes as high-performance anode materials for sodium ion batteries [J]. Journal of Materials Chemistry A, 2016, 4(15): 5505−5516.

[36] ZHANG Jia-feng, ZHANG Jian-yong, OU Xing, WANG Chun-hui, PENG Chun-li, ZHANG Bao. Enhancing high-voltage performance of Ni-rich cathode by surface modification of self-assembled NASICON fast ionic conductor $LiZr_2(PO_4)_3$ [J]. ACS Applied Materials & Interfaces, 2019, 11(17): 15507−15516.

# 氮掺杂碳包覆 $Bi_2Mn_4O_{10}$ 锂离子电池负极材料的制备及其电化学性能

湛 菁[1,2]，徐昌藩[1]，龙怡宇[1]，李启厚[1]

1. 中南大学 冶金与环境学院，长沙 410083；
2. 中南大学 难冶有色金属资源高效利用国家工程实验室，长沙 410083

**摘　要：**为抑制高能锂离子电池负极材料 $Bi_2Mn_4O_{10}$ 容量的快速衰减，通过简单球磨法制备新型高纯 $Bi_2Mn_4O_{10}$/ECP-N(ECP-N 为氮掺杂科琴黑)负极复合材料。所合成的 $Bi_2Mn_4O_{10}$/ECP-N 复合材料在 0.2*C* 倍率下循环 100 次后可保持 576.2 mA·h/g 的比容量，容量保持率为 75%，而纯 $Bi_2Mn_4O_{10}$ 的容量保持率仅为 27%。3*C* 倍率下 $Bi_2Mn_4O_{10}$/ECP-N 复合材料的放电容量仍保持在 236.1 mA·h/g。引入氮掺杂的科琴黑 ECP-N 不仅可以有效地提高比表面积以缓冲体积膨胀，增强材料的电导率和可湿性，而且还可以促进离子传输和可逆转化反应。

**关键词：**$Bi_2Mn_4O_{10}$ 纳米颗粒；氮掺杂科琴黑；倍率性能；锂离子电池

**(Edited by Wei-ping CHEN)**